coatings

MDPI

Article

Enhancement in the Electrochemical Performance of Strontium (Sr)-Doped $LaMnO_3$ as Supercapacitor Materials

Xin Ye [1], Songtao Dong [1,*], Xiaoyun Jin [1], Junlin Wei [1], Lei Wang [1] and Yamei Zhang [2,*]

[1] Institute of Material Science and Engineering, Jiangsu University of Science and Technology, Zhenjiang 212003, China
[2] School of Science, Jiangsu University of Science and Technology, Zhenjiang 212003, China
* Correspondence: stdong@just.edu.cn (S.D.); ymzhang@just.edu.cn (Y.Z.)

Abstract: In this study, Strontium (Sr)-doped perovskite lanthanum manganite ($La_{1-x}Sr_xMnO_3$) nanoparticles were prepared by the sol–gel method and used as electrode materials of supercapacitors. Microstructures, morphologies, and electrochemical properties of the samples were characterized by X-ray diffraction (XRD), scanning electron microscopy (SEM), a transmission electron microscope (TEM), Brunauer–Emmett–Teller (BET) surface area measurements, cyclic voltammetry (CV), and galvanostatic charge/discharge (GCD) cycling. Investigations demonstrated that the $La_{0.85}Sr_{0.15}MnO_3$ nanoparticles had a maximum specific capacitance of 185.5 F/g at a current density of 0.5 A/g and a low charge transfer resistance (0.38 Ω) in 3 M KOH aqueous electrolyte solutions. $La_{0.85}Sr_{0.15}MnO_3$ electrode yields the highest capacitance behavior because of the larger specific surface area, lower charge transfer resistance, and higher concentration of oxygen vacancy. This result demonstrates that Sr doping significantly improved the electrochemical properties of the $LaMnO_3$ system. The anion-intercalation mechanism was examined by a charge–discharge process. This provides a promising electrode material for supercapacitors.

Keywords: sol–gel method; $LaMnO_3$; electrode materials; electrochemical properties

check for updates

Citation: Ye, X.; Dong, S.; Jin, X.; Wei, J.; Wang, L.; Zhang, Y. Enhancement in the Electrochemical Performance of Strontium (Sr)-Doped $LaMnO_3$ as Supercapacitor Materials. *Coatings* **2022**, *12*, 1739. https://doi.org/10.3390/coatings12111739

Academic Editor: Je Moon Yun

Received: 8 October 2022
Accepted: 9 November 2022
Published: 13 November 2022

Publisher's Note: MDPI stays neutral with regard to jurisdictional claims in published maps and institutional affiliations.

Copyright: © 2022 by the authors. Licensee MDPI, Basel, Switzerland. This article is an open access article distributed under the terms and conditions of the Creative Commons Attribution (CC BY) license (https://creativecommons.org/licenses/by/4.0/).

1. Introduction

Due to the escalating global energy crisis and environmental pollution, the development of innovative and high-efficiency energy storage technologies has drawn substantial interest. To this end, electrochemical energy storage systems, such as lithium batteries and supercapacitors, offer enormous opportunities for lowering the use of fossil fuels and pollution [1–3] because of their quick discharging and charging times, significant power density, and extended cycle life. Specifically, supercapacitors have been identified as the best energy storage technology method, attracting substantial interest. However, compared to batteries, the practical applications of supercapacitors are limited because of their lower energy density. Therefore, considerable effort has been made toward the design of electrode materials for high-energy-density supercapacitors to address this limitation [4–6].

On the other hand, studies have shown that supercapacitor electrode materials considerably influence their electrochemical performance, prompting the extensive exploration of carbon compounds, conductive polymers, and metal oxides which have been extensively explored as electrochemical devices [7,8]. Among these compounds, metal oxides have attracted great interest because of their high energy concentration and more consistent electrochemical characteristics [9]. Metal oxides such as Ru_2O, MnO_2, $NiCo_2O_4$, Co_3O_4, V_2O_5, and Fe_3O_4 have also been considered as important primary materials because of their tunable surface morphology, different flexible oxidation states, and high structural stability [10–16]. Perovskite materials have become an important component in solid oxide fuel cells as well due to their excellent electrical and ionic properties [17]. Due to these materials having many oxygen vacancies that allow charge storage, their electronic and

ionic conductivity satisfy the requirements of supercapacitors; thus, perovskite materials are even more preferable as supercapacitor electrode materials.

In a previous study, Mefford et al. [18] reported the anion insertion technique for $LaMnO_3$ perovskite as a supercapacitor electrode material for the first time. Based on their findings, researchers have been drawn to lanthanide-based perovskite materials due to their excellent thermal stability, simple manufacturing, oxygen preservation, low price, and high electrical conductivity [19–21]. The oxygen vacancies in perovskites are considered as charge storage sites for pseudocapacitance [20]. Therefore, the energy densities of perovskite supercapacitors could be maximized by increasing the oxygen vacancies. The oxygen-vacancy concentration in perovskite oxides can be tailored by partial substitution on A-site and/or B-site, resulting in effective control over the crystal structure, electrical conductivity, and electrochemical performance [22–26]. Doping is an effective way to alter the oxygen vacancies in a $LaMnO_3$ matrix [22–25,27]. For instance, Ma et al. [24] showed that the specific capacitance of the $La_{0.85}Sr_{0.15}MnO_3$ electrode (129.0 mF/cm^2) was greater than that of $LaMnO_3$ (32.6 mF/cm^2). Then, Alexander et al. [28] used a low-valence A-site doping concept to synthesize $La_{1-x}Sr_xMnO_{3-\delta}$ perovskite materials with high charge storage, which proved that $La_{0.2}Sr_{0.8}MnO_{2.7}$ had the highest specific capacitance. Lu et al. [29] reported the results of a preliminary study of the pseudocapacitance features of strontium-doped lanthanum manganite. They reported no capacitance degradation after 1000 cycles and a specific capacitance of 56 F g^{-1} at a scan rate of 5 mV s^{-1}. The above-mentioned results show that Strontium (Sr) doping varied when $LaMnO_3$ had maximum specific capacitance. Therefore, exploring the impact of Sr doping on the electrochemical performance of $LaMnO_3$ perovskite materials is interesting and necessary.

Due to the sol–gel method with the advantages of rapid preparation of nanomaterials, it was easy to evenly and quantitatively incorporate some trace elements. To this end, the sol–gel method was used to create several $La_{1-x}Sr_xMnO_3$ (x = 0, 0.05, 0.1, 0.15, and 0.2) formulations, after which the impact of the properties and structural morphology of $La_{1-x}S_{rx}MnO_3$ (x = 0, 0.05, 0.1, 0.15, and 0.2) on its electrochemical performance was determined. Investigations revealed that 185.5 F/g was the highest specific capacitance of the investigated $La_{0.85}Sr_{0.15}MnO_3$ nanoparticles.

2. Experimental Section

2.1. Material Preparation

The specific experimental procedure for synthesizing the $La_{1-x}Sr_xMnO_3$ (x = 0.0, 0.05, 0.1, 0.15, and 0.2) samples using the sol–gel method is as follows: Firstly, the mass of the citric acid monohydrate (≥99.5%) is 0.4224 g, and the mass of $La(NO_3)_3{\cdot}6H_2O$ (≥99.9%), $MnCl_2{\cdot}4H_2O$ (≥99%), and $Sr(NO_3)_2$ (≥99.5%) according to stoichiometric ratios of $La_{1-x}Sr_xMnO_3$ were simultaneously solubilized in 30 mL of deionized water in turn and stirred for 24 h to obtain a clear solution. Next, the transparent solution was then dehydrated in an oven at 80°C for 72 h. Finally, the obtained solid powders were thoroughly ground, moved to a tube furnace, calcined in air at a heating rate of 5°C/min from room temperature to 700°C, and then held at 700°C for 2 h to yield $La_{1-x}Sr_xMnO_3$ (x = 0.0, 0.05, 0.1, 0.15, and 0.2).

2.2. Characterization

The thermal decomposition temperature of the samples was determined by employing a thermogravimetry analysis (Diamond TG/DTA, Perkin Elmer S. A., Waltham, MA, USA). First, with continuous ventilation, a part of every item weighing 4–6 mg was treated at 800 °C and a scan temperature of 15 °C min^{-1}. Then, the stages of generated nanoparticles were assessed through X-ray powder diffraction (D8 Advance, Bruker, Karlsruhe, Germany) with a checking width of 20°–60° and a reading speed of 6°/min. Subsequently, microstructures of materials were studied utilizing a field-emission scanning electron microscopy (FE-SEM, Merlin Compact, Carl Zeiss, Oberkochen, Germany) and a transmission electron microscope (TEM, 2100F, JEOL, Shoshima City, Japan). The Brunauer–Emmett–Teller (BET)

surface area and pore size distribution were measured using a N_2 adsorption–desorption physisorption analyzer (ASAP 2020, Micromeritics, Norcross, Ga, USA). The compositions' items, as well as molecular valency of the specimens, were evaluated through X-ray photoelectron spectroscopy (XPS, Thermo Fisher Scientific K-Alpha, Waltham, MA, USA). XPS with an Al K alpha X-ray source was used to examine the valance distributions of the samples.

2.3. Electrochemical Measurements

The active material (80 wt.%), acetylene black (10 wt%), and polyvinylidene fluoride (PVDF, 10 wt.%) were blended in N-methylpyrrolidone (NMP) for 24 h. The mass of the active materials used is 100 mg, and the volume of NMP is about 0.5 mL. A 1 mg active material was pasted onto carbon paper (1 cm × 1 cm) current collector and baked in a vacuum stove at 80 °C for 24 h to produce electrodes that need evaluation. Afterward, a three-electrode system with a Hg/HgO reference electrode, comprising a 3 M KOH mixture as the electrolyte, was utilized to investigate the electrochemical behavior of electrodes, followed by recordings of the electrochemical impedance spectra (EIS), cyclic voltammetric (CV) curves, and constant current charge–discharge (GCD) curves of the manufactured electrodes from an analyzer (CHI660E). The specific capacity of an electrode was calculated from the GCD curves using Equation (1):

$$C_s = \frac{I\Delta t}{m\Delta V} \quad (1)$$

where Cs is the specific capacitance (F g^{-1}), I is the specific current (A), Δt is the time for discharge (s), m is the mass of the active material (g), and ΔV is the potential range (V).

3. Results and Discussion

3.1. Microstructure and Morphology

While this study assessed the thermal decomposition temperature of $La_{1-x}Sr_xMnO_3$ precursors (x = 0.0, 0.05, 0.1, 0.15, and 0.2) using thermogravimetric assessment, that of the $LaMnO_3$ precursors were examined at an environment temperature of 50–800 °C with the temperature being increased at 15 °C/min. Figure 1a demonstrates the TG curve of the $LaMnO_3$ precursor. Investigations revealed a 15 wt.% drop in the weight of the $LaMnO_3$ precursors at 250 °C, mostly attributable to the evaporation of the natural solvents, gas, and humidity from the surface. At 380 °C, however, the precursor's weight reduced rapidly due to the breakdown of the citric acid monohydrate, $La(NO_3)_3{\cdot}6H_2O$, $MnCl_2{\cdot}4H_2O$, and $Sr(NO_3)_2$; then, at temperatures of more than 650 °C, the weight of the precursor remained unchanged. These findings indicate that thermal decomposition temperatures should exceed 650 °C. Therefore, a calcination temperature of 650 °C was adopted for the $La_{1-x}Sr_xMnO_3$ precursors. However, XRD studies indicated that $LaMnO_3$ was not synthesized, causing the calcination temperature to be raised to 700 °C, with subsequent XRD patterns proving that $LaMnO_3$ had been produced. In this investigation, $La_{1-x}Sr_xMnO_3$ precursors were thus synthesized at a calcination temperature of 700 °C.

On the other hand, Figure 1b illustrates the XRD system of $La_{1-x}Sr_xMnO_3$ (x = 0, 0.05, 0.1, 0.15, and 0.2) samples held at 700°C for 2 h. In contrast to the standard card (PDF 50–0297), all peaks at 23.0°, 32.6°, 40.1°, 46.7°, 52.7°, and 58.2°, which belonged to the (110), (200), (022), (220), (130), and (024) crystal planes, respectively, appeared to correlate with those of $LaMnO_3$; no additional peaks were visible. This finding suggests that samples of $La_{1-x}Sr_xMnO_3$ were achieved at the specified calcination temperature. Investigations also revealed that the (200) deviation peaks of $La_{1-x}Sr_xMnO_3$ examples moved to the left as the Sr doping concentration increased. In addition, per the Bragg formula, $2d\sin\theta = n\lambda$ (where d is the crystal plane area, θ is the angle of incidence, λ is the wavelength, and n is the count of reflection levels), the lattice constant of $La_{1-x}Sr_xMnO_3$ samples was also raised with increasing Sr doping because the ionic radius of Sr (1.18 Å) was greater than that of La (1.06 Å) [24].

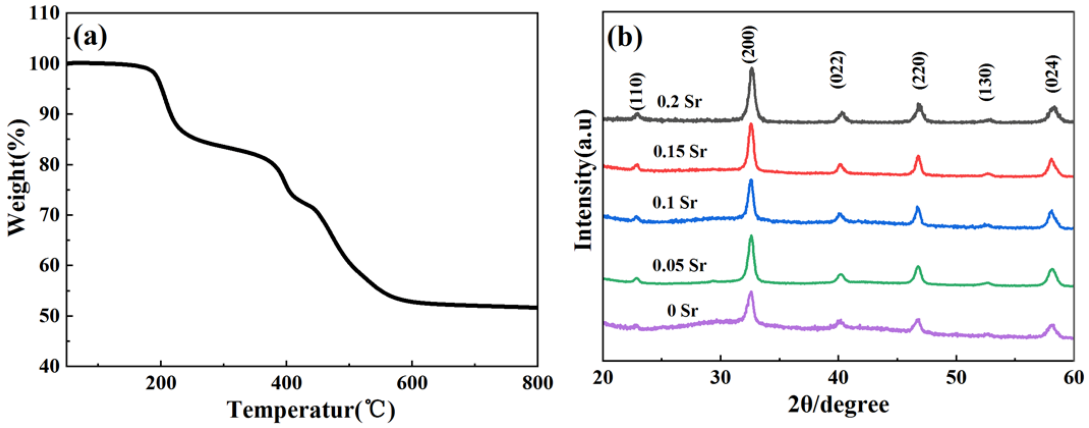

Figure 1. (**a**) TG curve of the $LaMnO_3$ precursor and (**b**) XRD pattern of $La_{1-x}Sr_xMnO_3$ (x = 0.0, 0.05, 0.1, 0.15, and 0.2).

In contrast, the morphologies of $La_{1-x}Sr_xMnO_3$ (x = 0.0, 0.05, 0.1, 0.15, and 0.2) specimens are illustrated in Figure 2a–e. The graphs demonstrate that the $La_{1-x}Sr_xMnO_3$ samples had a homogeneous particle distribution and tiny grain size; the grain sizes of the $La_{1-x}Sr_xMnO_3$ nanoparticles reduced as Sr doping increased because the lattice flaws in the $La_{1-x}Sr_xMnO_3$ nanoparticles rose as Sr doping increased, negatively affecting grain expansion and lowering grain size [30]. Subsequently, TEM was used to assess the effect of Sr doping on the $La_{1-x}Sr_xMnO_3$ nanoparticle's structure by characterizing the morphology of $LaMnO_3$ and $La_{0.85}Sr_{0.15}MnO_3$ samples. The results are shown in Figure 2f–i. Figure 2f,h shows that $LaMnO_3$ and $La_{0.85}Sr_{0.15}MnO_3$ samples comprised fine nanoparticle stacks with small grain sizes and uniform distribution; the grain size of the $La_{0.85}Sr_{0.15}MnO_3$ sample (~25 nm) was considerably smaller than that of the $LaMnO_3$ sample (~50 nm). Furthermore, the electron diffraction patterns of both the $LaMnO_3$ {Figure 2g} and $La_{0.85}Sr_{0.15}MnO_3$ {Figure 2i} samples showed concentric ring patterns, indicating the polycrystalline nature of the $LaMnO_3$ and $La_{0.85}Sr_{0.15}MnO_3$ samples. Then, the XRD data proposed that each ring can be assigned to various planes, as seen in the relevant images.

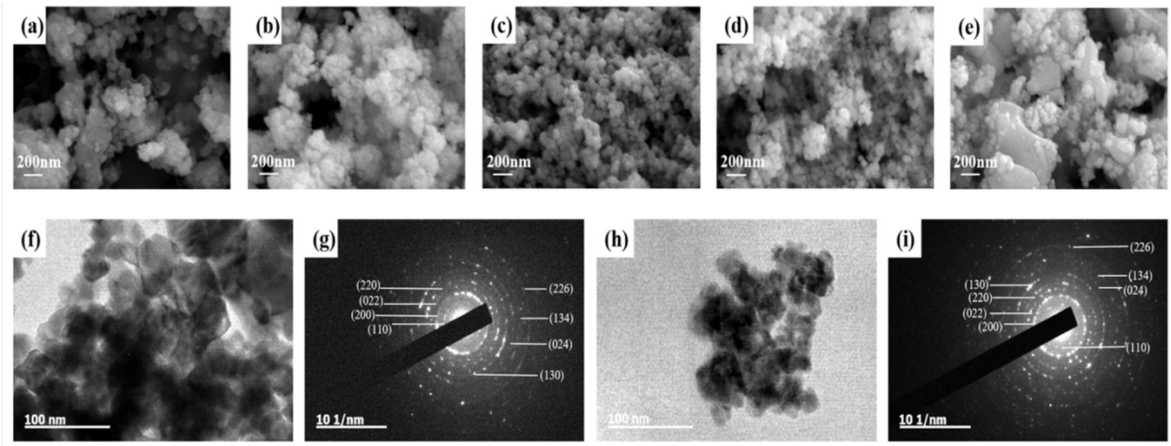

Figure 2. SEM images of (**a**) $LaMnO_3$, (**b**) $La_{0.95}Sr_{0.05}MnO_3$, (**c**) $La_{0.9}Sr_{0.1}MnO_3$, (**d**) $La_{0.85}Sr_{0.15}MnO_3$, and (**e**) $La_{0.8}Sr_{0.2}MnO_3$; (**f**,**g**) TEM image and selected area electron diffraction images of $LaMnO_3$; (**h**,**i**) TEM image and selected area electron diffraction patterns of $La_{0.85}Sr_{0.15}MnO_3$.

The surface area and pore size distribution of $La_{1-x}Sr_xMnO_3$ (x = 0.0, 0.05, 0.1, 0.15, and 0.2) nanoparticles were measured using a N_2 adsorption–desorption physisorption analyzer. Figure 3a,b depicts the isotherm description and orifice size distribution curve. Investigations revealed that the isothermal curves of the $La_{1-x}Sr_xMnO_3$ (x = 0.0, 0.05, 0.1, 0.15,

and 0.2) samples were a type IV hysteresis coil, indicating the mesoporous region of the synthesized samples [31]. Figure 3 shows the specific surface area and average pore diameters of $La_{1-x}Sr_xMnO_3$. The specific surface area of the $La_{0.95}Sr_{0.05}MnO_3$, $La_{0.9}Sr_{0.1}MnO_3$, $La_{0.85}Sr_{0.15}MnO_3$, and $La_{0.8}Sr_{0.2}MnO_3$ sample was 24.82, 29.61, 31.56, and 44.33 $m^2\ g^{-1}$, respectively, which is larger than that of the $LaMnO_3$ sample (22.25 $m^2\ g^{-1}$). The average pore diameters of the $LaMnO_3$, $La_{0.95}Sr_{0.05}MnO_3$, $La_{0.9}Sr_{0.1}MnO_3$, $La_{0.85}Sr_{0.15}MnO_3$, and $La_{0.8}Sr_{0.2}MnO_3$ samples were 2.81, 2.03, 2.04, 3.05, and 3.14 nm, respectively. Note that the $La_{0.85}Sr_{0.15}MnO_3$ sample had a larger specific surface area.

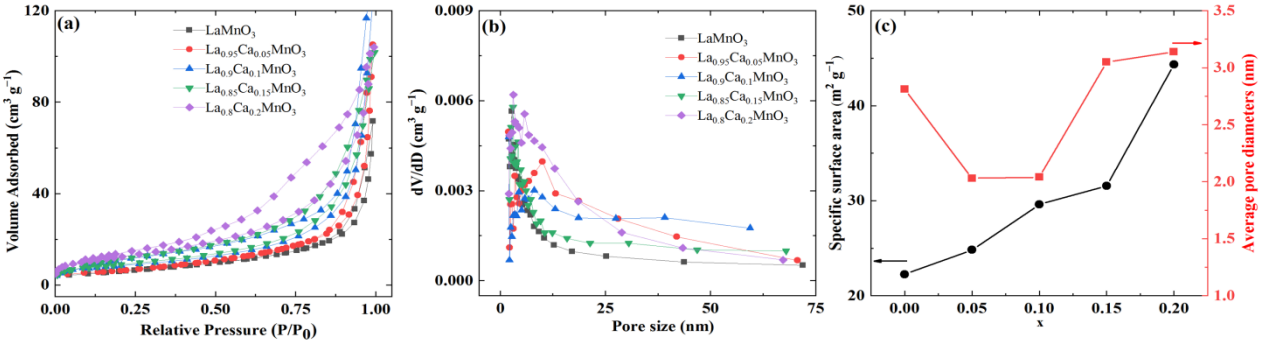

Figure 3. (**a**) N_2 adsorption–desorption isotherms of $La_{1-x}Sr_xMnO_3$ (x = 0.0, 0.05, 0.1, 0.15, and 0.2) nanoparticles, (**b**) BJH pore size distributions of $La_{1-x}Sr_xMnO_3$ (x = 0.0, 0.05, 0.1, 0.15, and 0.2) nanoparticles, (**c**) The specific surface area and average pore diameters of $La_{1-x}Sr_xMnO_3$ (x = 0.0, 0.05, 0.1, 0.15, and 0.2).

Figure 4 shows the oxidation states and composition of the $La_{1-x}Sr_xMnO_3$ (x = 0.0, 0.05, 0.1, 0.15, and 0.2) specimens. In particular, Figure 4a reveals the XPS survey scan, which indicated that the prepared samples included La, Sr, Mn, and O. However, Figure 4b displays the La 3d XPS spectra, with the peaks at 834.4 and 838 eV being the spin–orbit peaks of La $3d_{5/2}$ and including extra peaks at 850.8 and 855.4 eV representing that of La $3d_{3/2}$ [32]. These results indicate that La in $La_{1-x}Sr_xMnO_3$ was present in the +3 valence state, which is identical to the results reported by Zhang et al. [33]. On the other hand, the Mn 2p spectra of $La_{1-x}Sr_xMnO_3$ illustrated a wide outflow line width and a unique top range, confirming the existence of Mn in various oxidation conditions [34]. Accordingly, studies have widely utilized a simple tip-differential examination of Mn 2p to determine the manganese oxidation status of manganese with combined valences [22,24,35]. In contrast, Figure 4c illustrates the peak-differentiating evaluation of the Mn 2p spectra for the $La_{1-x}Sr_xMnO_3$ (x = 0.0, 0.05, 0.1, 0.15, and 0.2) samples. The two main peaks at 639.98 and 651.78 eV correlated with Mn $2p_{3/2}$ and Mn $2p_{1/2}$ [24], and the various numbers were kept at ~11.8 eV. Every peak was adjusted to three Mn oxidation states—Mn^{2+}, Mn^{3+}, and Mn^{4+}. Investigations also revealed that while the features of the peaks at 641.2 eV and 652.3 eV related to Mn^{2+}, those at 642.3 and 653.9 eV related to Mn^{3+}, and those at 644.0 and 655.5 eV related to Mn^{4+} [22]. Conversely, Figure 4d shows oxygen's high-resolution XPS spectra. The results illustrate that the three spikes adjusted to the greater fields in the O 1s part at 529.29, 530.9, and 533.1 eV correlated with O_1, O_2, and O_3 [32], where O_1 correlated with lattice oxygen (O^{2-}), O_2 correlated with the exterior extracted oxygen (O^-, O_2^-, and O_2^{2-}), and O_3 correlated with the oxygen-holding groups (OH). The proportional amounts of the three oxygen models are shown in Table 1. The oxygen molecules of the electrode items were inextricably connected with the conductivity, as well as the increased content of the O_2 types; the chemical absorption possibility of OH− became smoother, proposing that this connection optimized the activity of outward redox processes and their electrochemical qualities [36]. Furthermore, while the chemical oxygen vacancy of O_2^{2-} or O^- corresponded with oxygen deficiency, the density of oxygen vacancy was represented by the ratio of the area. The outside O_2/O_1 molar proportion reduced in the following arrangement: $La_{0.85}Sr_{0.15}MnO_3$ (1.34) > $La_{0.8}Sr_{0.2}MnO_3$ (1.3) > $La_{0.9}Sr_{0.1}MnO_3$ (1.16) >

$La_{0.95}Sr_{0.05}MnO_3$ (1.08) > $LaMnO_3$ (1.06), illustrating that $La_{0.85}Sr_{0.15}MnO_3$ had the highest electrochemical efficiency among the supercapacitors [37]. Finally, Figure 4e demonstrates the high-resolution XPS spectrum of Sr 3d, which revealed that the spike features at 131.08 and 132.8 eV correlated with the $3d_{5/2}$ and $3d_{3/2}$ spin–orbit peaks, confirming that the sample chemical valence state of Sr was +2 [38].

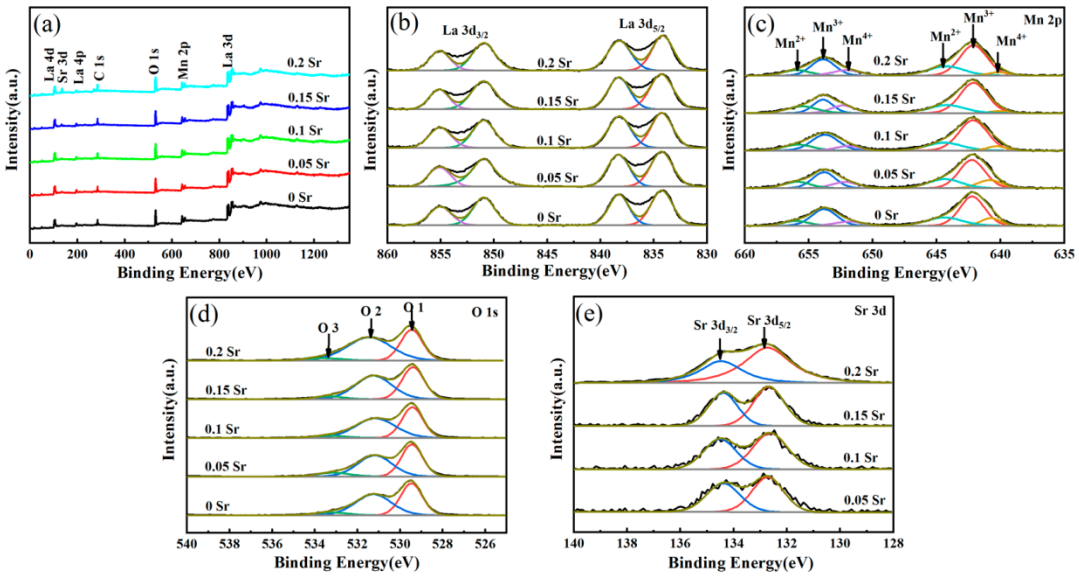

Figure 4. (**a**) XPS survey spectrum of $La_{1-x}Sr_xMnO_3$ (x = 0.0, 0.05, 0.1, 0.15, and 0.2); high-resolution spectrum of (**b**) La3d, (**c**) Mn2p, (**d**) O1s, and (**e**) Sr3d.

Table 1. The proportional density of the three oxygen molecules of O 1s in the $La_{1-x}Sr_xMnO_3$ (x = 0.0, 0.05, 0.1, 0.15, and 0.2) samples.

	$LaMnO_3$	$La_{0.95}Sr_{0.05}MnO_3$	$La_{0.9}Sr_{0.1}MnO_3$	$La_{0.85}Sr_{0.15}MnO_3$	$La_{0.8}Sr_{0.2}MnO_3$
O_1(%)	44.8	44.6	43.1	39.9	40.6
O_2(%)	47.6	48.3	50.1	53.6	52.8
O_3(%)	7.6	7.1	6.8	6.5	6.6

3.2. Electrochemical Properties

Figure 5 illustrates the CV curves of $La_{1-x}Sr_xMnO_3$ (x = 0.0, 0.05, 0.1, 0.15, and 0.2) electrodes at various testing voltage situations using 3 M KOH as the electrolyte. As the scan rate rose, the CV curves remained the same, suggesting great reversibility. However, the CV curves revealed a typical pseudocapacitor behavior, indicating a relationship between the maximum redox at 0.15 V and −0.15 V and a shift in the valence state of manganese ions from trivalent to divalent [22,24], respectively. Therefore, as per the anion insertion pathway, the redox reactions of $LaMnO_3$ during charging and discharging trials were illustrated as follows [24]:

$$La[Mn^{2+}_{2\delta};\ Mn^{3+}_{1-2\delta}]O_{3-\delta} + 2\delta OH^- \leftrightarrow LaMn^{3+}O_3 + 2\delta e^- + \delta H_2O \quad (2)$$

$$LaMn^{3+}O_3 + 2\delta OH^- \leftrightarrow La[Mn^{4+}_{2\delta};\ Mn^{3+}_{1-2\delta}]O_{3+\delta} + 2\delta e^- + \delta H_2O \quad (3)$$

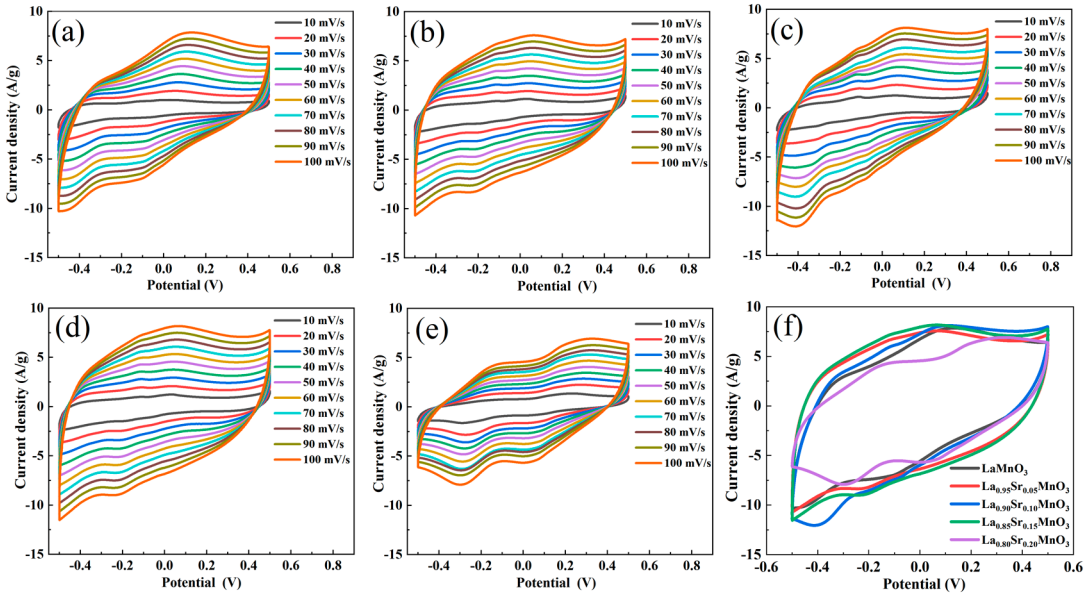

Figure 5. CV curves of $La_{1-x}Sr_xMnO_3$ (x = 0.0, 0.05, 0.1, 0.15, and 0.2): (**a**) $LaMnO_3$; (**b**) $La_{0.95}Sr_{0.05}MnO_3$; (**c**) $La_{0.9}Sr_{0.1}MnO_3$; (**d**) $La_{0.85}Sr_{0.15}MnO_3$; (**e**) $La_{0.8}Sr_{0.2}MnO_3$; (**f**) CVs recorded at a scan rate of 100 mV/s for all samples in 3 M KOH electrolyte.

The oxygen intercalation process in $LaMnO_3$ samples: First, $La\left[Mn_{2\delta}^{2+};Mn_{1-2\delta}^{3+}\right]O_{3-\delta}$ extracts OH^- from the electrolyte to create O^{2-} and H_2O. Then, O^{2-} is pushed into the perovskite lattice, thereby diffusing from t the borders of the O_2 octahedron and finally filling oxygen openings in the composition. As a result, the required Mn^{2+} changes to Mn^{3+} and finally creates a neutral $LaMn^{3+}O_3$. Second, manganese arises from the center of the oxygen octahedron, after which excessive oxygen is incorporated into the exterior, thus causing the generation of $La\left[Mn_{2\delta}^{4+};Mn_{1-2\delta}^{3+}\right]O_{3+\delta}$ [18]. Consequently, the divalent component (Sr^{2+}) replaces a part of La^{3+} in the A site due to the presence of extra oxygen vacancies. The reaction then changes to the following:

$$La_{0.85}Sr_{0.15}[Mn_{2\delta}^{2+};\ Mn_{1-2\delta}^{3+}]O_{2.925-\delta} + 2\delta OH^- \leftrightarrow La_{0.85}Sr_{0.15}Mn^{3+}O_{2.925} + 2\delta e^- + \delta H_2O \quad (4)$$

$$La_{0.85}Sr_{0.15}Mn^{3+}O_{2.925} + 2\delta OH^- \leftrightarrow La[Mn_{2\delta}^{4+};Mn_{1-2\delta}^{3+}]O_{2.925+\delta} + 2\delta e^- + \delta H_2O \quad (5)$$

For the $La_{0.85}Sr_{0.15}MnO_3$ samples, the oxidation process from Mn^{2+} to Mn^{3+} was similar to that of Mefford et al. [18], where the oxygen vacancy was filled by O^{2-} intercalation. Although all Mn^{2+} were oxidized to Mn^{3+}, $La_{0.85}Sr_{0.15}Mn^{3+}O_{2.925}$ remained hypoxic. Therefore, two stages were identified in the process of Mn^{3+} oxidation to Mn^{4+}. In the first stage, when $\delta \leq 0.075$, Mn^{3+} was oxidized to Mn^{4+} by constantly extracting O^{2-} to occupy the residual oxygen vacancies. As a result, many oxygen vacancies moved to the material surface to form $La_{0.85}Sr_{0.15}[Mn_{0.15}^{4+};Mn_{0.85}^{3+}]O_3(\delta = 0.075)$. The second stage is similar to that in $LaMnO_3$, in which the oxidation of Mn^{3+} to Mn^{4+} caused the formation of $La_{0.85}Sr_{0.15}[Mn_{2\delta}^{4+};Mn_{1-2\delta}^{3+}]O_{2.925+\delta}$.

Figure 5 shows that the $La_{1-x}Sr_xMnO_3$ (x = 0.0, 0.05, 0.1, 0.15, and 0.2) electrodes had a large voltage window (−0.5–0.5 V). As the Sr content rose, the closed area of the CV curves developed and eventually declined at the same scanning speed. $La_{0.85}Sr_{0.15}MnO_3$ had the largest closed region. However, when the sample was doped with Sr, the oxygen vacancies increased, in addition to the pseudocapacitance of the oxide, thereby increasing the specific capacitance value. The specific capacitance rose and dropped with increasing Sr doping levels due to the ion exchange process; the results are shown in Figure 5f. The process of oxygen admission may illustrate this capacity trend by raising Sr doping. As Sr doping increased, the concentrations of oxygen vacancies in the samples of Table 1 increased

and then decreased. This changing trend was consistent with the specific capacitance. Furthermore, while the different radii of Sr^{2+} and La^{3+} resulted in lattice mismatch, which decreased the tolerance factor, t, it also affected the perovskite structure, indicating that excessive Sr doping could result in the lattice distortion of $La_{1-x}Sr_xMnO_3$ because oxygen ions were not transported through the oxygen vacancies, which reduces the charge storage efficiency and specific capacitance [24]. Hence, increasing the specific surface area is useful for improving electrochemical performance.

Figure 6 shows the constant current charge–discharge (GCD) curves for the $La_{1-x}Sr_xMnO_3$ (x = 0.0, 0.05, 0.1, 0.15, and 0.2) electrodes at diverse current concentrations. Results revealed that the samples discharged faster as the charge–discharge current density rose. This finding was due to the fact that the specific capacitance decreased as the internal resistance rose with increasing current density. Consequently, the discharge time will be lowered. Alterations in the curve slope were also proposed to result from the alterations in the valence state from Mn^{2+} to Mn^{3+}. The specific capacitances of synthesized $La_{1-x}Sr_xMnO_3$ at a current density of 0.5 A/g are 67, 97, 115, 185.5, and 137.5 F/g, respectively. Figure 6f displays the specific capacitance of $La_{1-x}Sr_xMnO_3$ (x = 0.0, 0.05, 0.1, 0.15, and 0.2) as a function of current density. Due to the ion-exchange process, particular capacitance values fell as the current density rose, indicating that the trend of specific capacitance corresponded to the density of oxygen vacancies in the mechanism. These results also demonstrate that the capacitance of $La_{1-x}Sr_xMnO_3$ (x = 0.0, 0.05, 0.1, 0.15, and 0.2) specimens could be elevated by a La site exchange.

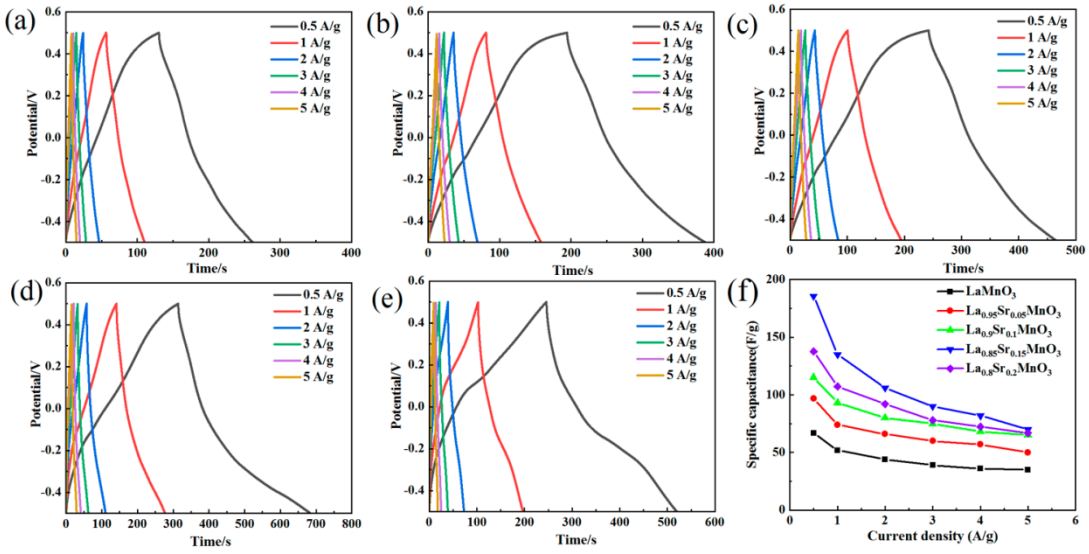

Figure 6. Charge–discharge curves of $La_{1-x}Sr_xMnO_3$ (x = 0.0, 0.05, 0.1, 0.15, and 0.2): (**a**) $LaMnO_3$; (**b**) $La_{0.95}Sr_{0.05}MnO_3$; (**c**) $La_{0.9}Sr_{0.1}MnO_3$; (**d**) $La_{0.85}Sr_{0.15}MnO_3$; (**e**) $La_{0.8}Sr_{0.2}MnO_3$; and (**f**) specific current against the specific capacitance of $La_{1-x}Sr_xMnO_3$.

Figure 7 shows the Nyquist plots of the $La_{1-x}Sr_xMnO_3$ (x = 0.0, 0.05, 0.1, 0.15, and 0.2) electrodes measured by EIS within the frequency variety of 100 kHz to 0.01 Hz. Generally, while impedance diagrams were divided into linear and semicircular parts, the semicircular curve region was in the AC impedance's high-frequency region, indicating that a redox reaction occurred on the electrode surface. Investigations also revealed that the straight-line region was in the low-frequency region of AC impedance, which shows the capacitive resistance generated at the electrode surface. Subsequently, the resistive range was adjusted to a circuit (displayed in the inset), usually containing an equivalent series resistance (R_s), charge transfer resistance (R_{ct}), Warburg element (W_o), and constant phase element (CPE). R_s is a combination of the electrolyte ionic resistance, the intrinsic resistance of active material, and the contact resistance between the active material and the current collector. According to the Nyquist plot, the R_{ct} values were 0.49, 0.47, 0.41, 0.38, and

4.4 Ω (as shown in Figure 7b), respectively, with the $La_{0.85}Sr_{0.15}MnO_3$ sample having a minimal charge transfer impedance, demonstrating excellent electrochemical features. Moreover, $La_{1-x}Sr_xMnO_3$ (x = 0.05, 0.1, 0.15, and 0.2), which had extra oxygen vacancies, was better for the insertion of oxygen than $LaMnO_3$, thus resulting in a smaller impedance to ion diffusion. Hence, these electrochemical records confirmed that the $La_{0.85}Sr_{0.15}MnO_3$ nanoparticles were favorable negative electrode materials for supercapacitors.

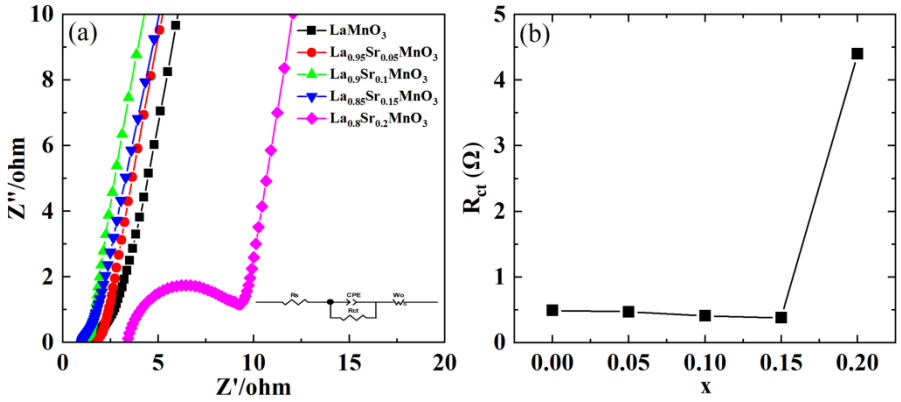

Figure 7. (**a**) The impedance comparison diagram of $La_{1-x}Sr_xMnO_3$ (x = 0.0, 0.05, 0.1, 0.15, and 0.2) electrodes; (**b**) The R_{ct} of $La_{1-x}Sr_xMnO_3$ (x = 0.0, 0.05, 0.1, 0.15, and 0.2) electrodes.

4. Conclusions

$La_{1-x}Sr_xMnO_3$ (x = 0.0, 0.05, 0.1, 0.15, and 0.2) nanoparticles were successfully synthesized using the sol–gel approach. As the Sr doping content increased, the grain size decreased, the specific surface area increased, and the density of oxygen vacancy in the $LaMnO_3$ regulation initially rose and then reduced, indicating that the particular capacitance of the $La_{1-x}Sr_xMnO_3$ nanoparticles followed a similar trend. Investigations also revealed that the $La_{0.85}Sr_{0.15}MnO_3$ nanoparticles with additional intrinsic oxygen vacancies demonstrated a maximum specific capacitance (185.5 F/g). This finding demonstrated that a particular capacitance of the $LaMnO_3$ system can be enhanced by La site substitution. As a result, this study successfully developed a potential electrode material for supercapacitor applications.

Author Contributions: Conceptualization and data curation, X.Y.; methodology and formal analysis, X.J.; investigation, J.W.; investigation, L.W.; writing—original draft preparation, S.D.; writing—review and editing, Y.Z. All authors have read and agreed to the published version of the manuscript.

Funding: This research was funded by the National Natural Science Foundation of China (Grant No. 51702132) and the Postgraduate Research & Practice Innovation Program of Jiangsu Province (Grant No. KYCX20_3132).

Institutional Review Board Statement: Not applicable.

Informed Consent Statement: Not applicable.

Data Availability Statement: Not applicable.

Acknowledgments: The authors acknowledge financial support from the National Natural Science Foundation of China (51702132). Song-Tao Dong acknowledges the open project of the National Laboratory of Solid State Microstructures at Nanjing University. Jun-Lin Wei acknowledges financial support from the Postgraduate Research & Practice Innovation Program of Jiangsu Province (Grant No. KYCX20_3132).

Conflicts of Interest: The authors declare that they have no conflict of interest.

References

1. Simon, P.; Gogotsi, Y.; Dunn, B. Where do batteries end and supercapacitors begin. *Science* **2014**, *343*, 1210–1211. [CrossRef]
2. Chu, S.; Majumdar, A. Opportunities and challenges for a sustainable energy future. *Nature* **2012**, *488*, 294–303. [CrossRef] [PubMed]
3. Zhong, C.; Deng, Y.; Hu, W.; Qiao, J.; Zhang, L.; Zhang, J. A review of electrolyte materials and compositions for electrochemical supercapacitors. *Chem. Soc. Rev.* **2015**, *44*, 7484–7539. [CrossRef] [PubMed]
4. Bose, S.; Kuila, T.; Mishra, A.K.; Rajasekar, R.; Kim, N.H.; Lee, J.H. Carbon-based nanostructured materials and their composites as supercapacitor electrodes. *J. Mater. Chem.* **2011**, *22*, 767–784. [CrossRef]
5. Snook, G.A.; Kao, P.; Best, A.S. Conducting-polymer-based supercapacitor devicesand electrodes. *J. Power Sources* **2011**, *196*, 1–12. [CrossRef]
6. Yuan, C.; Yang, L.; Hou, L.; Shen, L.; Zhang, X.; Lou, X.W.D. Growth of ultrathin mesoporous Co_3O_4 nanosheet arrays on Ni foam for high-performance electrochemical capacitors. *Energy Environ. Sci.* **2012**, *5*, 7883–7887. [CrossRef]
7. Wang, G.P.; Zhang, L.; Zhang, J.J. A review of electrode materials for electrochemical supercapacitors. *Chem. Soc. Rev.* **2012**, *41*, 797–828. [CrossRef]
8. Xue, Q.; Sun, J.; Huang, Y.; Zhu, M.; Pei, Z.; Li, H.; Wang, Y.; Li, N.; Zhang, H.; Zhi, C. Recent progress on flexible and wearable supercapacitors. *Small* **2017**, *13*, 1701827. [CrossRef] [PubMed]
9. Chen, H.; Jiang, G.; Yu, W.; Liu, D.; Liu, Y.; Li, L.; Huang, Q.; Tong, Z. Electrospun carbon nanofibers coated with urchinlike $ZnCo_2O_4$ nanosheets as a flexible electrode material. *J. Mater. Chem.* **2016**, *4*, 5958–5964. [CrossRef]
10. Zhu, Y.; Ji, X.; Pan, C.; Sun, Q.; Song, W.; Fang, L.; Chen, Q.; Banks, C.E. A carbon quantum dot decorated RuO_2 network: Outstanding supercapacitances under ultrafast charge and discharge. *Energy Environ. Sci.* **2013**, *6*, 3665–3675. [CrossRef]
11. Chang, J.K.; Huang, C.H.; Tsai, W.T.; Deng, M.J.; Sun, I.-W. Ideal pseudocapacitive performance of the Mn oxide anodized from the nanostructured and amorphous Mn thin film electrodeposited in BMP-NTf2 ionic liquid. *J. Power Sources* **2008**, *179*, 435–440. [CrossRef]
12. Zhang, G.; Lou, X.W. Controlled Growth of $NiCo_2O_4$ Nanorods and Ultrathin Nanosheets on Carbon Nanofibers for High-Performance Supercapacitors. *Sci. Rep.* **2013**, *3*, 1470–1475. [CrossRef] [PubMed]
13. Wang, B.; Zhu, T.; Wu, H.B.; Xu, R.; Chen, J.S.; Lou, X.W. Porous Co_3O_4 nanowires derived from long $Co(CO_3)_{0.5}(OH)_{0.11}H_2O$, nanowires with improved supercapacitive properties. *Nanoscale* **2012**, *4*, 2145–2149. [CrossRef] [PubMed]
14. Pan, A.Q.; Wu, H.B.; Zhang, L.; Lou, X.W. Uniform V_2O_5 nanosheet-assembled hollow microflowers with excellent lithium storage properties. *Energy Environ. Sci.* **2013**, *6*, 1476–1479. [CrossRef]
15. Wu, Z.S.; Yang, S.; Sun, Y.; Parvez, K.; Feng, X.; Müllen, K. 3D nitrogen-doped graphene aerogel-supported Fe_3O_4 nanoparticles as efficient electrocatalysts for the oxygen reduction reaction. *J. Am. Chem. Soc.* **2012**, *134*, 9082–9085. [CrossRef]
16. Hussain, S.; Javed, M.S.; Ullah, N.; Shaheen, A.; Aslam, N.; Ashraf, I.; Abbas, Y.; Wang, M.; Liu, G.; Qiao, G. Unique hierarchical mesoporous $LaCrO_3$ perovskite oxides for highly efficient electrochemical energy storage applications. *Ceram. Int.* **2019**, *45*, 15164–15170. [CrossRef]
17. Jin, T.; Wang, X.; Jiao, L. Recent progress in electrospinning method for secondary ion batteries and electrocatalysis. *Sci. Sin. Chim.* **2019**, *49*, 692–703. [CrossRef]
18. Mefford, J.T.; Hardin, W.G.; Dai, S.; Johnston, K.P.; Stevenson, K.J. Anion charge storage through oxygen intercalation in $LaMnO_3$ perovskite pseudocapacitor electrodes. *Nat. Mater.* **2014**, *13*, 726–732. [CrossRef]
19. Ho, K.H.; Wang, J. Hydrazine reduction of $LaNiO_3$ for active materials in supercapacitors. *J. Am. Ceram. Soc.* **2017**, *100*, 4629–4637. [CrossRef]
20. Elsiddig, Z.A.; Xu, H.; Wang, D.; Zhang, W.; Guo, X.; Zhang, Y.; Sun, Z.; Chen, J. Modulating Mn^{4+} ions and oxygen vacancies in nonstoichiometric $LaMnO_3$ perovskite by a facile sol–gel method as high-performance supercapacitor electrodes. *Electrochim. Acta* **2017**, *253*, 422–429. [CrossRef]
21. Ma, P.P.; Zhu, B.; Lei, N.; Liu, Y.K.; Yu, B.; Lu, Q.L.; Dai, J.M.; Li, S.H.; Jiang, G.H. Effect of Sr substitution on structure and electrochemical properties of perovskite-type $LaMn_{0.9}Ni_{0.1}O_3$ nanofibers. *Mater. Lett.* **2019**, *252*, 23–26. [CrossRef]
22. Mo, H.Y.; Nan, H.S.; Lang, X.Q.; Liu, S.J.; Qiao, L.; Hu, X.Y.; Tian, H.W. Influence of calcium doping on performance of $LaMnO_3$ supercapacitors. *Ceram. Int.* **2018**, *44*, 9733–9741. [CrossRef]
23. Zhang, Y.H.; Zhu, X.B.; Wei, B.; Lv, Z.; Huang, Q. Strontium doped lanthanum manganite/manganese dioxide composite electrode for supercapacitor with enhanced rate capability. *Electrochim. Acta* **2016**, *222*, 1585–1591.
24. Ma, P.P.; Lu, Q.L.; Lei, N.; Liu, Y.K.; Yu, B.; Dai, J.M.; Li, S.H.; Jiang, G.H. Effect of A-site substitution by Ca or Sr on the structure and electrochemical performance of $LaMnO_3$ perovskite. *Electrochim. Acta* **2020**, *332*, 135489. [CrossRef]
25. Lv, J.; Zhang, Y.; Zhe, L.; Huang, X.; Wang, Z.; Bo, W. Strontium doped lanthanum manganite (LSM) effects on electrochemical performance of LSM/MnO_2 composites for supercapacitor. *J. Mater. Sci. Mater. Electron.* **2017**, *28*, 17020–17025. [CrossRef]
26. Rezanezhad, A.; Rezaie, E.; Ghadimi, L.S.; Hajalilou, A.; Abouzari-Lotf, E.; Arsalani, N. Outstanding supercapacitor performance of Nd-Mn co-doped perovskite $LaFeO_3$@nitrogen-doped graphene oxide nanocomposites. *Electrochim. Acta* **2020**, *335*, 135699. [CrossRef]
27. Younis, A.; Loucif, A. Defects mediated enhanced catalytic and humidity sensing performance in ceria nanorods. *Ceram. Int.* **2021**, *47*, 15500–15507. [CrossRef]

28. Alexander, C.T.; Mefford, J.T.; Saunders, J.; Forslund, R.P.; Johnston, K.P.; Stevenson, K.J. Anion-based pseudocapacitance of the perovskite library $La_{1-x}Sr_xBO_{3-\delta}$ (B = Fe, Mn, Co). *ACS Appl. Mater. Interfaces* **2019**, *11*, 5084–5094. [CrossRef]
29. Lu, J.; Zhang, Y.; Lu, Z.; Huang, X.; Wang, Z.; Zhu, X.; Wei, B. A preliminary study of the pseudo-capacitance features of strontium doped lanthanum manganite. *RSC Adv.* **2015**, *5*, 5858. [CrossRef]
30. Cao, Y.; Lin, B.P.; Sun, Y.; Yang, H.; Zhang, X.Q. Synthesis, structure and electrochemical properties of lanthanum manganese nanofibers doped with Sr and Cu. *J. Alloys Compd.* **2015**, *638*, 204–213. [CrossRef]
31. Jiang, R.R.; Wang, Y.K.; Cheng, W.; Yu, S.; Zhang, J.M. Hollow $ZnSnO_3$/reduced graphene oxide ternary composite as anode of lithium ion batteries with enhanced electrochemical performance. *Ceram. Int.* **2017**, *43*, 11556–11562. [CrossRef]
32. Nagamuthu, S.; Vijayakumar, S.; Ryu, K. Cerium oxide mixed $LaMnO_3$ nanoparticles as the negative electrode for aqueous asymmetric supercapacitor devices. *Mater. Chem. Phys.* **2017**, *199*, 543–551. [CrossRef]
33. Sunding, M.F.; Hadidi, K.; Diplas, S.; Lovvik, O.M.; Norby, T.E.; Gunnæs, A.E. XPS characterisation of in situ treated lanthanum oxide and hydroxide using tailored charge referencing and peak fifitting procedures. *J. Electron. Spectrosc. Relat. Phenom.* **2011**, *184*, 399–409. [CrossRef]
34. Najjar, H.; Batis, H. Development of Mn-based perovskite materials: Chemical structure and applications. *Catal. Rev.* **2016**, *58*, 371–438. [CrossRef]
35. Zhu, Q.; Zhao, D.; Cheng, M.; Zhou, J.; Owusu, K.A.; Mai, L.; Yu, Y. A new view of supercapacitors: Integrated supercapacitors. *Adv. Energy Mater.* **2019**, *33*, 1901081. [CrossRef]
36. Yan, D.; Wang, W.; Luo, X.; Chen, C.; Zeng, Y.; Zhu, Z. $NiCo_2O_4$ with oxygen vacancies as better performance electrode material for supercapacitor. *Chem. Eng. J.* **2018**, *334*, 864–872. [CrossRef]
37. Tian, H.W.; Lang, X.Q.; Nan, H.S.; An, P.; Zhang, W.; Hu, X.Y.; Zhang, J.S. Nanosheet-assembled $LaMnO_3$@$NiCo_2O_4$ nanoarchitecture growth on Ni foam for high power density supercapacitors. *Electrochim. Acta* **2019**, *318*, 651–659. [CrossRef]
38. Komai, S.; Hirano, M.; Ohtsu, N. Spectral analysis of Sr 3d XPS spectrum in Sr-containing hydroxyapatite. *Surf. Interface Anal.* **2020**, *52*, 823–828. [CrossRef]